JGR Planets

RESEARCH ARTICLE
10.1029/2023JE008032

Key Points:

- Mercury's disappearing dayside magnetosphere event under extreme solar wind conditions is studied by using 3-D global hybrid simulations
- Most of the dayside magnetosphere, even the dayside bow shock, disappears shortly after the interaction between the extreme solar wind and the planetary magnetic field
- Ion precipitation on the planetary surface and the time evolution of magnetopause standoff distance under different solar wind conditions are also studied

Correspondence to:
S. Lu and Q. Lu,
lusan@ustc.edu.cn;
qmlu@ustc.edu.cn

Citation:
Guo, J., Lu, S., Lu, Q., Slavin, J. A., Sun, W., Ren, J., et al. (2023). Three-dimensional global hybrid simulations of Mercury's disappearing dayside magnetosphere. *Journal of Geophysical Research: Planets*, *128*, e2023JE008032. https://doi.org/10.1029/2023JE008032

Received 27 JUL 2023
Accepted 4 DEC 2023

© 2023. American Geophysical Union. All Rights Reserved.

Three-Dimensional Global Hybrid Simulations of Mercury's Disappearing Dayside Magnetosphere

Jin Guo[1,2], San Lu[1,2,3], Quanming Lu[1,2,3], James A. Slavin[4], Weijie Sun[4,5], Junyi Ren[1,2,3], Xueyi Wang[6], Yu Lin[6], Rajkumar Hajra[1,2,3], and Rongsheng Wang[1,2,3]

[1]School of Earth and Space Sciences, University of Science and Technology of China, Hefei, China, [2]CAS Center for Excellence in Comparative Planetology/CAS Key Lab of Geospace Environment, University of Science and Technology of China, Hefei, China, [3]Collaborative Innovation Center of Astronautical Science and Technology, Harbin, China, [4]Department of Climate and Space Sciences and Engineering, University of Michigan, Ann Arbor, MI, USA, [5]Space Science Laboratory, University of California, Berkeley, CA, USA, [6]Physics Department, Auburn University, Auburn, AL, USA

Abstract An important discovery of MESSENGER is the occurrence of dayside disappearing magnetosphere (DDM) events that occur when the solar wind dynamic pressure is extremely high and the interplanetary magnetic field (IMF) is both intense and southward. In this study, we investigate the DDM events at Mercury under extreme solar wind conditions using a three-dimensional (3-D) global hybrid simulation model. Our results show that when the solar wind dynamic pressure is 107 nPa and the magnitude of the purely southward IMF is 50 nT, most of the dayside magnetosphere disappears within 10 s after the interaction between the solar wind and the planetary magnetic field starts. During the DDM event, the ion flux is significantly enhanced at most of the planetary dayside surface and reaches its maximum value of about 10^{10} cm^{-2} s^{-1} at the low-latitude surface, which is much larger than that under normal solar wind conditions. During the DDM events, the dayside bow shock mostly disappears for about 9 s and then reappears. Moreover, the time evolution of magnetopause standoff distance under different solar wind conditions is also studied. When the solar wind dynamic pressure exceeds 25 nPa and the IMF is purely southward, a part of the dayside magnetosphere disappears. Under the same IMF, the higher the solar wind dynamic pressure, the faster the magnetopause standoff distance reaches the planetary surface. When the solar wind conditions are normal (with a dynamic pressure of 8 nPa) or the IMF is purely northward, the dayside magnetosphere does not disappear. The results provide a clear physical image of DDM events from a 3-D perspective.

Plain Language Summary Mercury has a significant, and apparently global, magnetic field. The planetary magnetic interacts with the solar wind originating from the Sun, creating a magnetosphere. However, it has been observed that the dayside part of the planetary magnetosphere can disappear, which is referred to as dayside disappearing magnetosphere (DDM) events. These events normally occur when the solar wind dynamic pressure is extremely high and the magnetic field in the solar wind is both intense and southward. In this study, we use computer simulations to investigate the DDM events at Mercury under extreme solar wind conditions. Our results show that most of the dayside magnetosphere disappears after the interaction between the extreme solar wind and the planetary magnetic field, leading to a significant enhancement in the precipitation of ion flux on the planetary surface. Moreover, the temporal evolution of the dayside magnetosphere's size under different solar wind conditions was also studied. Under the same solar wind magnetic field, the higher the solar wind dynamic pressure, the smaller the magnetosphere. The results provide a clear physical image of DDM events from a 3-D perspective.

1. Introduction

A major scientific discovery during the Mariner 10's flybys of Mercury was that the planet has a weak intrinsic magnetic field (less than 1% of Earth's magnetic field, Ness et al., 1974). The magnetic field measurements from the MErcury Surface, Space ENvironment, GEochemistry, and Ranging mission (MESSENGER) spacecraft, launched in 2004, revealed that Mercury's dipolar magnetic moment is closely aligned with its rotation axis and has a northward offset of about 0.2 times the radius of Mercury (R_M, which is 2,440 km) (Alexeev et al., 2010; Anderson et al., 2011). This magnetic offset leads to notable north-south asymmetries in both the polar magnetic field and the size of the polar caps (Korth et al., 2018). The weak intrinsic magnetic field of Mercury interacts with the solar wind, forming a miniature magnetosphere with a typical magnetopause standoff distance of about

$1.5R_M$ from the center of Mercury's internal magnetic dipole (Winslow et al., 2013). This miniature magnetosphere effectively shields the planet from the direct impact of solar wind particles. Many physical phenomena during the solar wind-magnetosphere interaction, such as flux transfer event (FTE) showers at the magnetopause (Lu et al., 2022; Slavin et al., 2012; Sun et al., 2020), ultra-low frequency waves in the foreshock (Le et al., 2013; Romanelli & DiBraccio, 2021; Romanelli et al., 2020), ring current in the inner magnetosphere (Shi et al., 2022; Zhao et al., 2022), Kelvin-Helmholtz waves in the magnetospheric flanks (Gershman et al., 2015; Liljeblad et al., 2014; Slavin et al., 2008; Sundberg et al., 2011), very fast reconnection, more than three times faster than that observed at Earth (DiBraccio et al., 2013; Slavin et al., 2009), and dawn-dusk asymmetries in the magnetotail reconnection (Liu et al., 2019; Smith et al., 2017; Sun et al., 2016), have been widely studied.

Mercury possesses a large-size, electrically conducting iron core with a radius of approximately $0.8R_M$ (e.g., Smith et al., 2012), which distinguishes it from other planets in the solar system. The electromagnetic coupling between Mercury's conducting core and its space environment has significant effects on the solar wind-magnetosphere interaction (e.g., Hood & Schubert, 1979; Suess & Goldstein, 1979). Under varying solar wind conditions, the position of Mercury's magnetopause changes relative to the planetary surface. The magnetopause motion and the corresponding changes of the current system lead to magnetic field perturbations within Mercury's interior and near its surface, causing induced currents in the conducting core (Heyner et al., 2016; Slavin et al., 2014). The induced currents further produce magnetic fields that can constitute a significant fraction of Mercury's weak intrinsic field (Glassmeier et al., 2007). Hence, the magnetic field induced by the currents in the planetary core enhances the dipolar magnetic field of Mercury and provides a shield for the planet, limiting the direct impact of the solar wind particles on the planetary surface (Dong et al., 2019; Jia et al., 2015, 2019).

During major coronal mass ejection impacts, the dayside magnetosphere of Mercury can be highly compressed (Jia et al., 2019; Slavin et al., 2014) and even "disappear" (Slavin et al., 2019; Winslow et al., 2020; Zhong et al., 2015). These intervals are termed "disappearing dayside magnetosphere" (DDM) events. Slavin et al. (2019) examined four low-altitude MESSENGER passes over the dayside hemisphere of Mercury for which no dayside magnetosphere, only magnetosheath was observed. Such events, or ones similar to them, have been noted previously by Zhong et al. (2015) and Winslow et al. (2020) but not analyzed in detail. These magnetospheric responses to the upper ranges solar wind dynamic pressures and southward interplanetary magnetic field (IMF) intensity in the MESSENGER observations at Mercury have been divided into two categories: highly compressed magnetosphere (HCM) events and DDM events. HCM events are characterized by magnetospheric magnetic field intensities just inside of the subsolar magnetopause of >300 nT and correspond to solar wind dynamic pressures in the MESSENGER data of approximately 40–90 nPa (Jia et al., 2019). The magnetopause crossings during the HCM events were analyzed in the MESSENGER data and were found to have significant normal magnetic fields to the magnetopause despite 7 of the 8 events having magnetic shear angles across the magnetopause less than 90° (Jia et al., 2019). The DDM events, in contrast, are associated with more severe upstream dynamic pressures of about 140–290 nPa (Slavin et al., 2019), respectively. The MESSENGER DDM magnetopause crossings appeared to present only at very high latitudes, about 66–80°, just sunward of the day-night terminator plane. The magnetic fields in the dayside DDM magnetosheath were very intense and strongly southward, B_z about −100 to −400 nT (Slavin et al., 2019).

These observations indicate that the extreme solar wind compression and reconnection-driven erosion of Mercury's dayside magnetosphere lead to the DDM events. Due to the limited observations from the MESSENGER spacecraft, it is difficult to study the DDM events in detail, such as the three-dimensional (3-D) shape and time evolution of Mercury's magnetosphere and the ion flux precipitating on the planetary surface. Although various numerical models, including global magnetohydrodynamic (MHD) (Jia et al., 2015, 2019; Kabin, 2000; Kabin et al., 2008; Kidder et al., 2008; Varela et al., 2015) and Hall MHD (Li et al., 2023), hybrid models (Exner et al., 2018, 2020; Fatemi et al., 2020; Kallio & Janhunen, 2003; Müller et al., 2012; Trávníček et al., 2007, 2010; Wang et al., 2010), and particle-in-cell model (Lapenta et al., 2022), have been performed to study the space environment of Mercury, DDM events still have not been studied using simulations.

Additionally, Potter and Morgan (1985) discovered abundant Na vapor in the planetary exosphere, with an estimated total column abundance of 8.1×10^{11} atoms cm^{-2}. They proposed that the source of Na could be ion sputtering, where ions originate from the solar wind or Mercury's magnetosphere. However, McGrath et al. (1986) estimated that the average Na column abundance resulting from ion sputtering under normal solar wind conditions is more than three orders of magnitude lower than the observed value. Hence, it is worth investigating whether ion sputtering can account for the source of Na during the DDM event.

In this study, we investigate the DDM events at Mercury under extreme solar wind conditions using a 3-D global hybrid simulation model. The simulation results demonstrate that most of the dayside magnetosphere disappears within 10 seconds after the interaction between the planetary magnetic field and the solar wind with extreme dynamic pressure and intense southward IMF. Due to the disappearance of the dayside magnetosphere, the ion flux at Mercury's surface is significantly enhanced compared to that under normal solar wind conditions. Due to this enhanced solar wind absorption as it impacts Mercury's surface, most of the dayside bow shock disappears until the initiation of the magnetotail reconnection. The dayside bow shock reappears once the magnetotail reconnection returns magnetic flux to the dayside magnetosphere. Moreover, we also examine the time evolution of magnetopause standoff distance under different solar wind conditions. The results provide a clear physical image of DDM events from a 3-D perspective and demonstrate how the Dungey cycle (Dungey, 1961) of magnetic flux circulation operates under extreme solar wind and IMF conditions in this small magnetosphere.

2. Simulation Model

A 3-D global hybrid code, named general curvilinear particle-in-cell (gcPIC) hybrid for Mercury, is used to simulate the DDM events at Mercury. The gcPIC is a software package that can implement kinetic simulations, including full particle simulation and hybrid simulation, in a general curvilinear coordinate system. The software package has previously been successfully used to study the excitation of chorus waves in a dipole magnetic field (Lu et al., 2019) and the FTE showers at Mercury (Lu et al., 2022). Hybrid simulation has been shown to be suitable for studying the planetary magnetosphere on a global scale (Guo et al., 2021, 2022). In the hybrid code, ions are treated as particles, and electrons are treated as a massless fluid, assuming quasi-charge neutrality. The hybrid simulation model adopts the Mercury Solar Orbital (MSO) coordinate system, where the $+x$ axis points to the Sun (i.e., the solar wind flows along the $-x$ axis), the $+y$ axis is opposite to the orbital motion of Mercury around the Sun and points toward dusk, and the $+z$ axis points to the geographical north. The simulation domain size is $-7R_M \le x \le 3R_M$, $-3R_M \le y \le 3R_M$, and $-5R_M \le z \le 5R_M$. Cartesian coordinates are used in the calculations. In this hybrid simulation model, Mercury is assumed to be a spherical object without an exosphere, and particles are absorbed at the planetary surface. Conducting boundary conditions for electromagnetic fields are applied at the inner boundary ($r = 0.55R_M$).

In the space environment ($r > 1R_M$), the electric field $\boldsymbol{E}$ is obtained from the massless electron momentum equation:

$$\boldsymbol{E} = -\boldsymbol{V}_e \times \boldsymbol{B} - (1/N)\nabla p_e - \upsilon(\boldsymbol{V}_e - \boldsymbol{V}_i), \tag{1}$$

where $\boldsymbol{B}$ is the magnetic field, N is the total ion number density, $\boldsymbol{V}_i$ is the total ion bulk flow velocity, $\boldsymbol{V}_e$ is the electron bulk flow velocity obtained from Ampere's law, ∇p_e is the electron pressure gradient, and υ is an ad hoc current-dependent collision frequency used to simulate the anomalous resistivity. The electron fluid is assumed to be isothermal, with a constant temperature T_e, and $\nabla p_e = T_e \nabla N$. The magnetic field is advanced in time by Faraday's law

$$\frac{\partial \boldsymbol{B}}{\partial t} = -\nabla \times \boldsymbol{E}. \tag{2}$$

Inside the planet ($0.55R_M < r \le 1R_M$), where the plasma convection is neglected, the bulk flow velocity of ions and the $(1/N)\nabla p_e$ are set to zero. Therefore, the magnetic field equation inside the planet becomes a pure diffusion equation:

$$\frac{\partial \boldsymbol{B}}{\partial t} = -\nabla \times \boldsymbol{E} = -\nabla \times \left(\frac{\eta}{\mu_0}\nabla \times \boldsymbol{B}\right), \tag{3}$$

where η is the resistivity. According to the previous studies (Dong et al., 2019; Jia et al., 2015), the resistivity η is $10^{-5}\,\Omega$ m within the conducting core ($0.55R_M < r \le 0.8R_M$) and $10^{7}\,\Omega$ m in the insulated mantle ($0.8R_M < r \le 1R_M$).

Mercury's dipole moment is set to 190 nT R_M^3 along the z-direction, with a $0.2R_M$ offset northward from the center of the planet (Anderson et al., 2011). Initially, the dipole magnetic field is confined to $x \le 2R_M$ by adding an image dipole. A uniform solar wind carrying a steady IMF is filled in the region $x > 2R_M$ with the front side boundary at $x = 3R_M$. Outflow boundary conditions are used at $x = -7R_M$, $y = \pm 3R_M$ and $z = \pm 4R_M$. A nonuniform

Table 1
Seven Simulation Cases With Different Solar Wind Conditions Chosen in This Study

Case	1	2	3	4	5	6	7
$\boldsymbol{B}_{sw}$ (nT)	(0, 0, −50)	(0, 0, −34)	(0, 0, −34)	(0, 0, −34)	(0, 0, 34)	(0, 0, −34)	From (0, 0, −34) to (0, 0, −50)
N_{i0} (cm^{-3})	100	80	60	40	60	From 40 to 60	From 40 to 100
$\boldsymbol{V}_{sw}$ (km/s)	(−800, 0, 0)	(−650, 0, 0)	(−500, 0, 0)	(−350, 0, 0)	(−500, 0, 0)	From (−350, 0, 0) to (−500, 0, 0)	From (−350, 0, 0) to (−800, 0, 0)
P_{dyn0} (nPa)	107	56	25	8	25	From 8 to 25	From 8 to 107
M_A	7.3	7.8	5.2	3.0	5.2	From 3.0 to 5.2	From 3.0 to 7.3
β	0.24	0.41	0.31	0.21	0.31	From 0.21 to 0.31	From 0.21 to 0.24
d_i (km)	22.8	25.4	29.4	36.0	29.4	From 36.0 to 29.4	From 36.0 to 22.8
$N_x \times N_y \times N_z$	676 × 382 × 560	676 × 382 × 560	587 × 274 × 494	587 × 274 × 494	587 × 274 × 494	587 × 274 × 494	676 × 382 × 560
Number of particles	~7.2 × 10^9	~7.2 × 10^9	~4.8 × 10^9	~4.8 × 10^9	~4.8 × 10^9	~4.8 × 10^9	~7.2 × 10^9

Note. $\boldsymbol{B}_{sw}$ is the IMF; N_{i0} is the solar wind number density; $\boldsymbol{V}_{SW}$ is the solar wind speed; P_{dyn0} is the dynamic pressure in the solar wind; M_A is the Mach number; β is the ratio of the plasma thermal pressure to the magnetic pressure in the solar wind; d_i is the solar wind ion inertial length, and $N_x \times N_y \times N_z$ is the number of grids. Note that Case 6 has time-varying solar wind conditions. These solar wind parameters are from Jia et al. (2019) and are estimated by the observation of MESSENGER.

grid cell system is employed, with a grid size of $(\Delta x, \Delta y, \Delta z) \approx (1d_i, 1.5d_i, 1d_i)$ (d_i is the solar wind ion inertial length) in the near-Mercury regions with $-2R_M < x < 2R_M$, $-2R_M < y < 2R_M$, and $-2R_M < z < 2R_M$ and a lower resolution in the lobes. The solar wind conditions, as well as the number of grids and particles in each case, are shown in Table 1. In Case 1, the solar wind conditions are extreme, while in Case 4, the solar wind conditions are normal. Note that in Case 6, the dynamic pressure in the solar wind changes from 8 to 25 nPa about 100 s after the simulation begins; in Case 7, the solar wind dynamic pressure increases from 8 to 107 nPa about 23 s after the simulation begins. Other plasma parameters are also time varying in this case. The time step Δt is chosen as 0.008-0.02 Ω_i^{-1}, where Ω_i is the ion gyrofrequency based on the IMF intensity.

3. Simulation Results

3.1. Extreme Solar Wind Condition (Case 1)

In Case 1, the dynamic pressure of the solar wind is chosen to be 107 nPa, and the magnitude of purely southward IMF is 50 nT, representing an extreme solar wind condition. The solar wind parameters were chosen based on their proximity to the observations in Slavin et al. (2019), their ability to reduce the computational resources required (higher dynamic pressure necessitates higher grid resolution), and their facilitation of intercomparisons among the individual simulation cases. The magnetotail is well formed at about $t = 45$ s, and the standoff distance of the dayside bow shock is steady. Figure 1 shows the 3-D views of Mercury's magnetopause at $t = 56.8$ s in Case 1. The white surface represents the 3-D magnetopause, while the region with enhanced plasma density is the magnetosheath. The bow shock is located between the solar wind and the magnetosheath. Due to the northward offset of the internal dipole, both the magnetopause and the magnetotail are shifted northward (refer to Figures 1b and 1c). In Figure 1, most of the dayside magnetosphere disappears, allowing particles from the magnetosheath to directly impact the planetary surface. About 26% of the dayside surface of Mercury is in contact with the magnetosheath. The standoff distance of the dayside bow shock (at $z = 0.2R_M$) is merely about $1.3R_M$, which is very close to the planetary surface. It also compares favorably with the $1.5R_M$ mean stand-off distance derived from fitting the location of the bow shock during the 4 DDM events in the Slavin et al. (2019) MESSENGER study.

Figure 2 illustrates the evolution of the magnetosphere and bow shock in Case 1. Due to the strong dynamic pressure in the solar wind, the dayside magnetosphere becomes highly compressed at $t = 8.38$ s (Figures 2a and 2e), resulting in the formation of intense Chapman-Ferraro currents at the magnetopause. The compression by the solar wind induces currents at the surface of the planetary core, leading to the formation of two current circuits that generate an induced magnetic field to prevent the compression. This result is consistent with previous simulation models for Mercury (Dong et al., 2019; Jia et al., 2015). At $t = 17.69$ s (Figures 2b and 2f), most of the dayside magnetosphere disappears, and the induced current circuits at the surface of the planetary core also

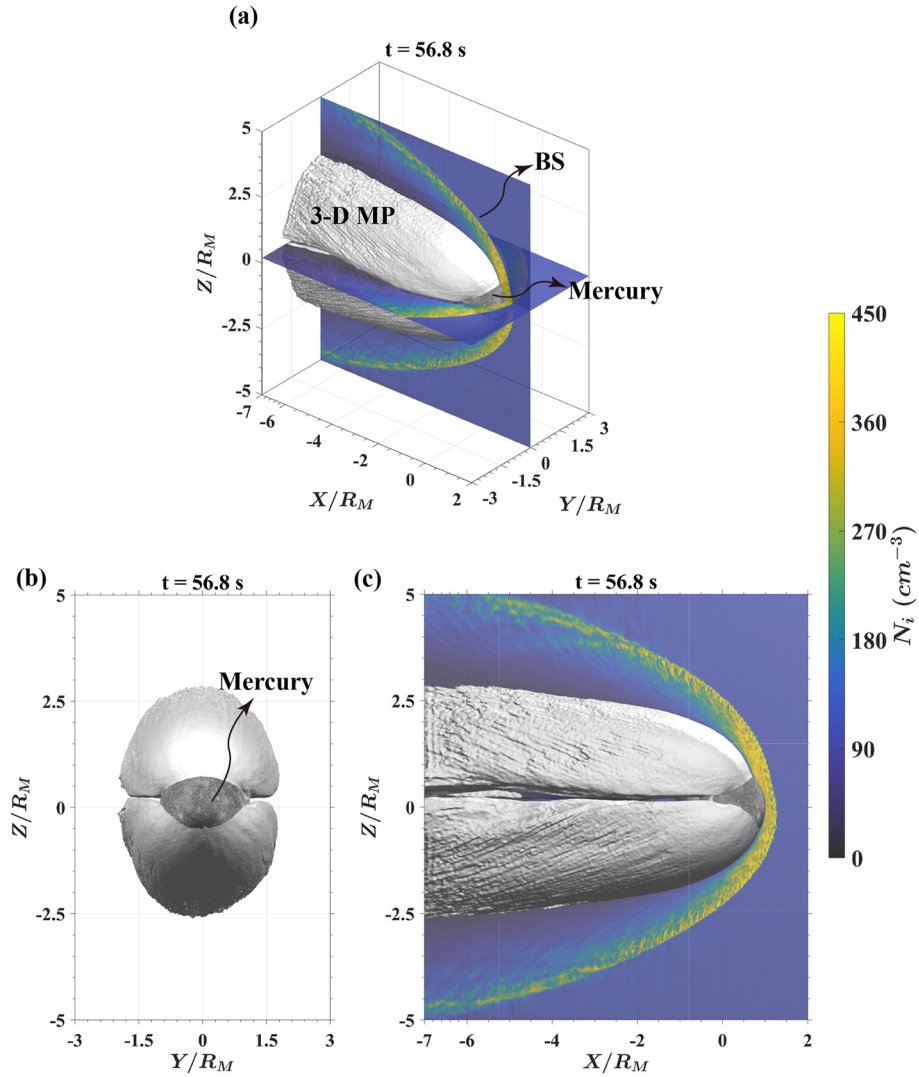

Figure 1. 3-D views of Mercury's magnetopause at $t = 56.8$ s obtained from Case 1. (a) The slices show the ion number density, N_i, in the noon-midnight meridian and equatorial planes. Mercury is indicated by a dark gray sphere. The 3-D magnetopause (3-D MP) is indicated by the white surface and is defined by the parameter $\beta^* = (P_{th} + P_{dyn})/P_{mag}$, where P_{th} is the plasma thermal pressure and P_{mag} is the magnetic pressure. The value range of β^* between 0.1 and 1.5, which was demonstrated by Brenner et al. (2021), is used to define the magnetopause. In this study, $\beta^* = 0.1$ is utilized to define the 3-D magnetopause, consistent with Ala-Lahti et al. (2022). (b) Views of the magnetopause from the direction of sunlight. (c) Views of the magnetopause from dawn to dusk.

disappear. Additionally, most of the dayside bow shock also disappears at this time, indicating that the solar wind particles can directly impact the surface of Mercury without being decelerated by the bow shock. At $t = 26.42$ s (Figures 2c and 2g), the magnetotail is formed, triggering magnetotail reconnection and resulting in the return of the magnetic flux from the magnetotail to the dayside magnetosphere. Therefore, the dayside bow shock is reappearing at this time. Finally, at $t = 56.8$ s (Figures 2d and 2h), the dayside bow shock reappears completely, while the dayside magnetosphere remains disappeared. The dayside bow shock disappears for about 9 s. The occurrence time of disappearing dayside magnetosphere and bow shock is much shorter than the Dungey cycle time scale of Mercury, ~2 min (Slavin, Anderson, et al., 2010).

To better illustrate the phenomenon of the disappearing dayside bow shock, Figure 3 plots the 3-D views of the bow shock (magenta surface) at two specific times, $t = 17.69$ and 56.8 s, in Case 1. In Figure 3a, most of the dayside bow shock disappears at $t = 17.69$ s, causing about 20% of the dayside surface of Mercury to be impacted directly by the solar wind. However, at $t = 56.8$ s, once the magnetotail is fully formed and the magnetic flux returns to the dayside magnetosphere, the dayside bow shock reappears completely (Figure 3b).

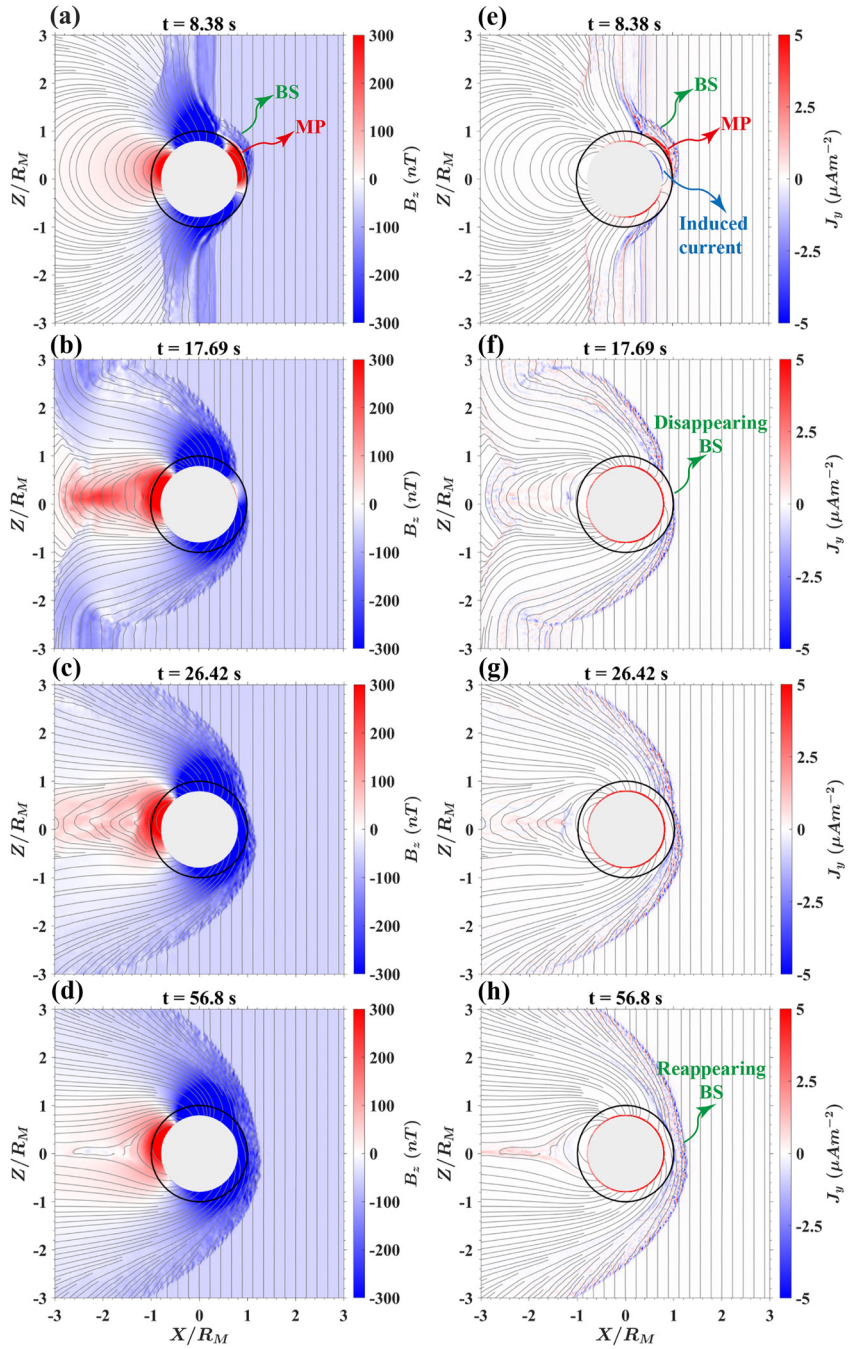

Figure 2. The evolution of the magnetopause and the bow shock in the noon-midnight meridian plane obtained from Case 1. (a–d) The magnetic field lines and the z component of magnetic field, B_z, at t = 8.38 s, 17.69 s, 26.42 s, and 56.8 s. (e–h) The magnetic field lines and the y component of current density J_y at the same time points. The green arrow denotes the location of the bow shock, while the red arrow indicates the position of the magnetopause. The blue arrow indicates the induced currents at the core surface of Mercury. The surface of Mercury is represented by a black circle, and the core of Mercury is represented by a gray circular region.

Figure 4 illustrates the ion flux at the planetary surface at t = 56.8 s in Case 1. Due to the disappearance of the dayside magnetosphere, the ion flux is significantly enhanced at most of the dayside surface (Figure 4a) and reaches its maximum value of about 10^{10} cm^{-2} s^{-1} at the low-latitude surface. In the nightside hemisphere (Figure 4b), the ion flux at the surface is mainly provided by the outflow of the magnetotail reconnection. The highest peak of the ion flux, about 10^9 cm^{-2} s^{-1}, occurs at the high latitudes of both the northern and southern

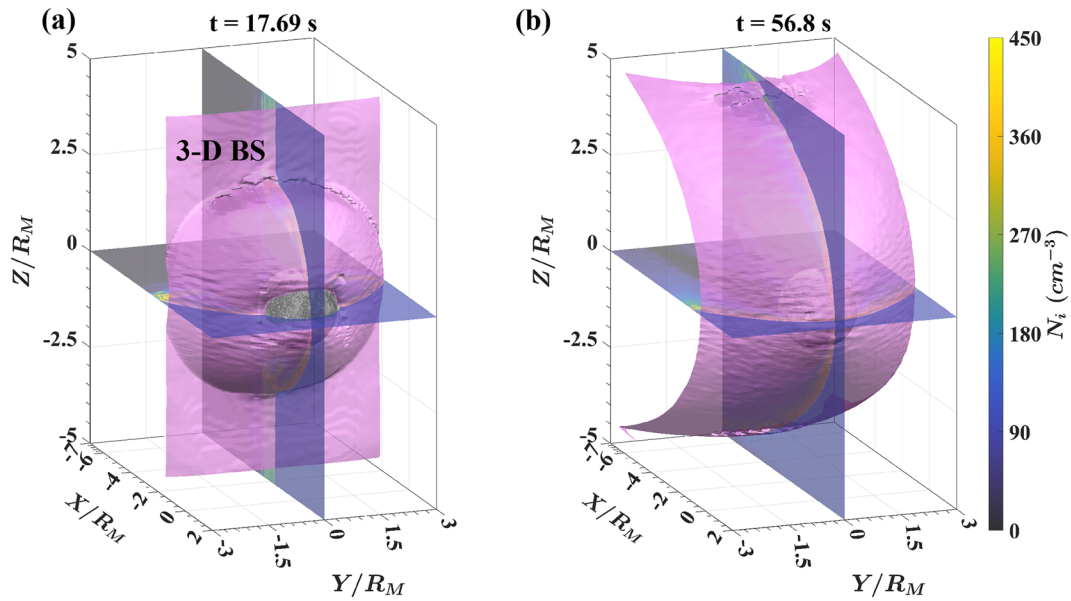

Figure 3. 3-D views of the bow shock at $t = 17.69$ and 56.8 s obtained from Case 1. The slices show the ion number density, N_i, in the noon-midnight meridian and equatorial planes at (a) $t = 17.69$ and (b) 56.8 s, respectively. The 3-D bow shock is indicated by the magenta surface in each panel and is identified by locating the highest gradient of the total velocity.

hemispheres, while the ion flux at low latitudes is merely about 10^7 cm^{-2} s^{-1}. This is because at high latitudes there are open magnetic field lines that map to the region just inside the separatrix layers formed by reconnection, allowing particles to precipitate onto the planetary surface. However, at the low latitudes, there are close field lines that provide a shield for the planetary surface against direct plasma impact. The total ion precipitation rate in the dayside hemisphere is 4.3×10^{26} s^{-1}, while in the nightside hemisphere, it is 4.1×10^{25} s^{-1}.

3.2. Normal Solar Wind Condition (Case 4)

In Case 4, as a comparison case, the dynamic pressure and the magnitude of IMF (purely southward) in the solar wind are chosen to be 8 nPa and 34 nT, respectively, to represent normal solar wind conditions. The magnetotail is well formed at about $t = 105$ s. Figure 5 shows the 3-D views of Mercury's magnetopause at $t = 135.56$ s in Case 4, with the white surface representing the 3-D magnetopause. The magnetosheath is the region with enhanced ion density. In this case, the dayside magnetosphere does not disappear. The standoff distances of the dayside magnetopause and bow shock (at $z = 0.2R_M$) are about $1.15R_M$ and $1.85R_M$, respectively. The bow shock to the

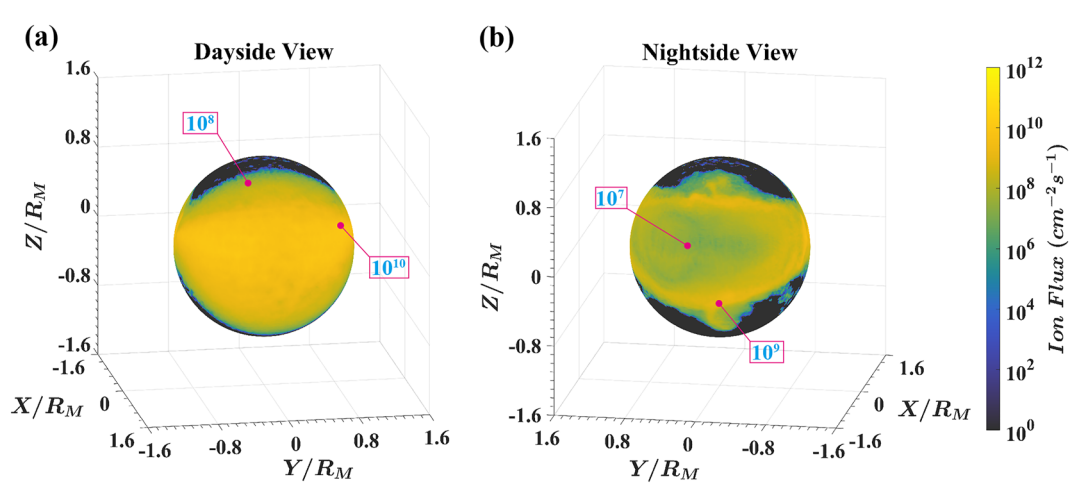

Figure 4. 3-D views of ion flux at Mercury's surface at $t = 56.8$ s obtained from Case 1. (a) View of dayside hemisphere. (b) View of nightside hemisphere.

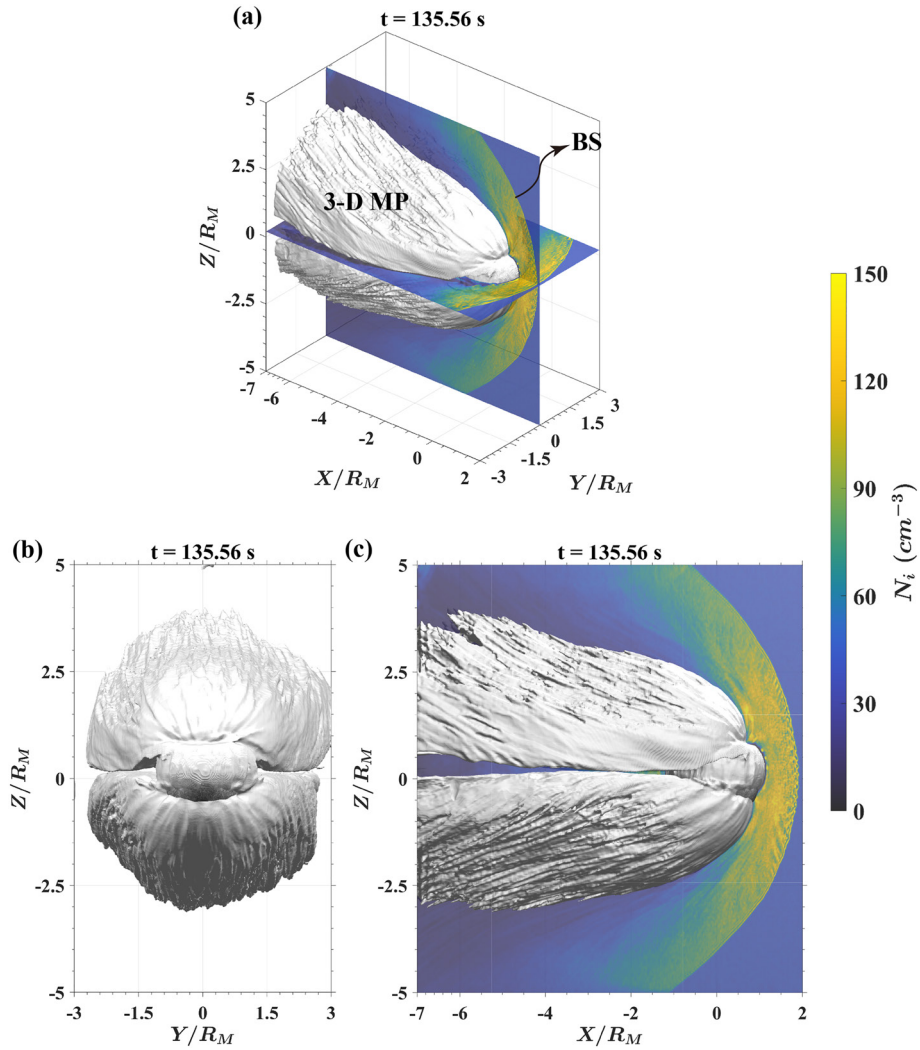

Figure 5. 3-D views of Mercury's magnetopause at $t = 135.56$ s obtained from Case 4. The rest are in the same format as Figure 1.

magnetopause standoff distance ratio is approximately 1.6 for a Mach number of 3. However, at Earth, this ratio is only around 1.3 for a relatively high Mach number ranging from 8 to 10 (Spreiter et al., 1966).

Figure 6 plots the ion flux at the planetary surface at $t = 135.56$ s under normal solar wind conditions (Case 4). In the dayside hemisphere (Figure 6a), there is a region characterized by low ion flux because the dayside magnetosphere blocks particles from the solar wind. However, in the cusp regions, the ion flux can reach up to about 10^9 cm^{-2} s^{-1}, which is consistent with the observation by Raines et al. (2022). Due to the northward offset of the internal dipole, the southern cusp region is larger than the northern cusp region. In the nightside hemisphere, the peak of ion flux (about 10^8 cm^{-2} s^{-1}) is at the high latitudes of both the northern and southern hemispheres, while the ion flux at low latitudes is about 10^6 cm^{-2} s^{-1}. The total ion precipitation rate in the dayside hemisphere is 2.9×10^{25} s^{-1}, which is consistent with the observed values (Poh et al., 2016; Sun et al., 2022). In the nightside hemisphere, the total ion precipitation rate is 1.3×10^{25} s^{-1}. It is noted that the total ion precipitation rate in the dayside hemisphere under normal solar wind conditions (Case 4) is more than an order of magnitude less than that under the extreme solar wind conditions shown in Case 1.

3.3. DDM Events Under Different Solar Wind Conditions

To determine how long it takes for DDM events to occur and the solar wind conditions under which DDM events occur, Figure 7 shows the temporal evolution of the magnetopause standoff distance in Cases 2–5. In Cases

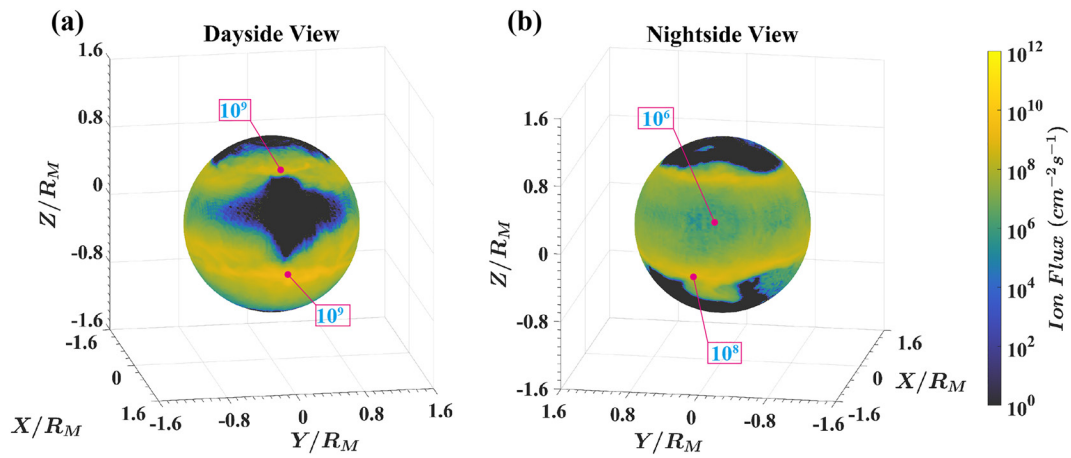

Figure 6. 3-D views of ion flux at Mercury's surface at $t = 56.8$ s obtained from Case 4. (a) View of dayside hemisphere. (b) View of nightside hemisphere.

2–4, only the dynamic pressure in the solar wind is changed (see Table 1), while the IMF is the same. In Case 2 (red line), with a dynamic pressure of 56 nPa in the solar wind, the magnetopause standoff distance reaches the minimum value of about $1.03R_M$ at $t = 8$ s (indicated by the red dashed vertical line). This represents the time taken for the conducting core to respond to changes in the magnetopause position. During the response time (8 s), the magnetic field perturbations generated by the motion of magnetopause are transported at the Alfvén speed toward the planetary surface, and the Alfvén wave then reflects at the core surface and is transported back to the magnetopause. Subsequently, the magnetopause standoff distance gradually increases due to the induced magnetic field produced by the currents at the core surface. The maximum value of the magnetopause standoff distance reaches up to $1.09R_M$ at $t = 12$ s. However, the dayside magnetopause is eroded by the magnetopause reconnection, causing the magnetopause standoff distance to reach $1R_M$ at $t = 27$ s. This implies that part of the dayside magnetosphere disappears. In Case 3 (green line), with a dynamic pressure of 25 nPa in the solar wind, the magnetopause standoff distance reaches its minimum value of about $1.11R_M$ at $t = 10$ s (indicated by the green dashed vertical line) when the induced currents at the core surface are well formed. Then, the magnetopause standoff distance gradually increases to $1.16R_M$ at $t = 16$ s and reaches $1R_M$ at $t = 58$ s, indicating that part of the dayside magnetosphere has also disappeared. In Case 4 (gray line), as shown in Section 3.2, the dynamic pressure in the solar wind is 8 nPa, which represents a normal solar wind condition (Sun et al., 2021). The minimum value of the magnetopause distance of about $1.27R_M$ occurs at $t = 14$ s (indicated by the gray dashed vertical

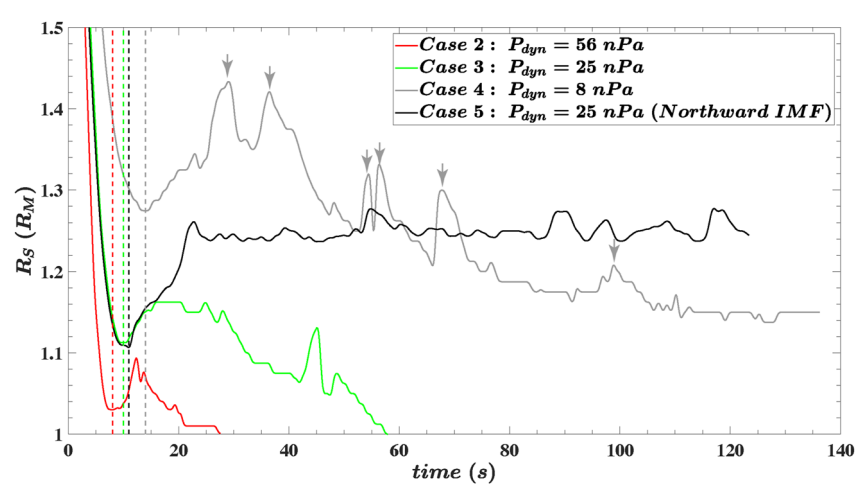

Figure 7. Temporal evolution of the magnetopause standoff distance, R_s, at $z = 0.2R_M$ obtained from Cases 2–4. The dashed lines with different colors indicate the points in time when the induced currents are well formed. The gray arrows in Case 4 indicate large FTEs formed at the dayside magnetopause.

line), when the induced currents at the core surface are well formed. Then, the magnetopause standoff distance gradually increases to $1.43R_M$ at $t = 29$ s. The peaks of the magnetopause standoff distance, indicated by the gray arrows, represent large-scale FTEs at the magnetopause. These large FTEs have a scale size of about $0.3–0.5R_M$ in agreement with MESSENGER in situ measurement of the larger FTEs (Slavin, Lepping, et al., 2010). After the formation of a large FTE, the magnetopause standoff distance significantly decreases, indicating that the large-scale FTEs have a pronounced effect on the erosion of the planetary dayside magnetosphere. At about $t = 100$ s, the magnetotail is well formed, and the magnetic flux returns to the dayside magnetosphere. The magnetopause standoff distance stabilizes at about $1.15R_M$.

Case 5, with a purely northward IMF, is performed to study the influence of the IMF direction while keeping other solar wind conditions the same as Case 3. The minimum magnetopause standoff distance of about $1.11R_M$ occurs at $t = 11$ s (indicated by the black dashed vertical line), which is the same as that in Case 3. Nevertheless, the magnetopause standoff distance stabilizes at about $1.25R_M$ after $t = 23$ s because of the absence of dayside magnetopause reconnection. Thus, it can be inferred that a strong solar wind dynamic pressure and a magnetopause reconnection significantly contribute to the disappearance of the dayside magnetosphere.

3.4. Effect of Return Flux on DDM Events

The return flux formed by the magnetotail reconnection or driven by the magnetopause reconnection is found to replenish the dayside magnetosphere (Juusola, Østgaard, & Tanskanen, 2011; Juusola, Østgaard, Tanskanen, Partamies, & Snekvik, 2011; Sun et al., 2017). In Cases 1–3, with dynamic pressure ranging from 25 to 107 nPa in the solar wind, the dayside magnetosphere disappears prior to the formation of the magnetotail. One issue is that if there is no magnetotail and the return flux at the beginning, it may be easy for the dayside magnetosphere to disappear. To address this issue, we perform another simulation with time-varying solar wind conditions (Case 6). Before $t = 100$ s, the solar wind dynamic pressure is 8 nPa; to ensure the formation of the magnetotail, after $t = 100$ s, the solar wind dynamic pressure increases to 25 nPa. Figure 8 shows the evolution of Mercury's magnetosphere in Case 6. At $t = 73.94$ s (Figures 8a and 8d), the magnetotail begins to form, and the magnetopause stabilizes at about $1.15R_M$ (at $z = 0.2R_M$). When the solar wind with enhanced dynamic pressure impacts the dayside magnetosphere at $t = 101.67$ s (Figures 8b and 8e), the dayside magnetosphere becomes significantly compressed. Finally, at $t = 127.4$ s (Figures 8c and 8f), there are no closed magnetic field lines on the dayside hemisphere, which is consistent with the results of Case 3. From this case study (Case 6), it can be inferred that the return flux from the magnetotail under normal solar wind conditions cannot prevent the disappearance of the magnetosphere. Therefore, the solar wind dynamic pressure of Cases 1 and 2 is 107 and 56 nPa, respectively, and the return flux from the magnetotail under normal solar wind conditions is even more unable to prevent the disappearance of the dayside magnetosphere.

4. Discussion

To avoid the influence of initialization on Case 1, we perform Case 7 with time-varying solar wind conditions. Before $t = 23.11$ s (Figures 9a and 9e), the solar wind dynamic pressure is 8 nPa, and the magnetopause has been formed at $t = 23.11$ s. Since the magnetopause is formed, the simulation is not initialized in a particular manner. After $t = 23.11$ s, the solar wind dynamic pressure increased to 107 nPa. Due to the strong dynamic pressure in the solar wind, the dayside magnetosphere becomes highly compressed at $t = 30.81$ s (Figures 9b and 9f). At $t = 37.13$ s (Figures 9c and 9g), most of the dayside magnetosphere and the dayside bow shock disappear within 14 s after the arrival of the extreme solar wind. At $t = 44.06$ s (Figures 9d and 9h), the dayside bow shock reappeared. The dayside bow shock disappears for about 7 s. These results are similar to those in Case 1 that initialized in a particular manner. Therefore, the influence of initialization on simulations is minimal.

Mercury is too small and hot for its gravity to retain a significant atmosphere. However, it does have a thin exosphere that is bound to the planetary surface. The atoms in the exosphere collide with the surface or escape from the planet, rather than colliding with each other. The first investigation of Mercury's exosphere came with the Mariner 10 flybys, where atomic hydrogen, helium, and oxygen were discovered using ultraviolet photometers (Broadfoot et al., 1976). Potter and Morgan (1985) later discovered strong emission features in the spectrum of Mercury at the Fraunhofer sodium (Na) D lines using ground-based telescopes and spectrometers. These emission features are attributed to the resonant scattering of sunlight from Na vapor in the planetary exosphere. The

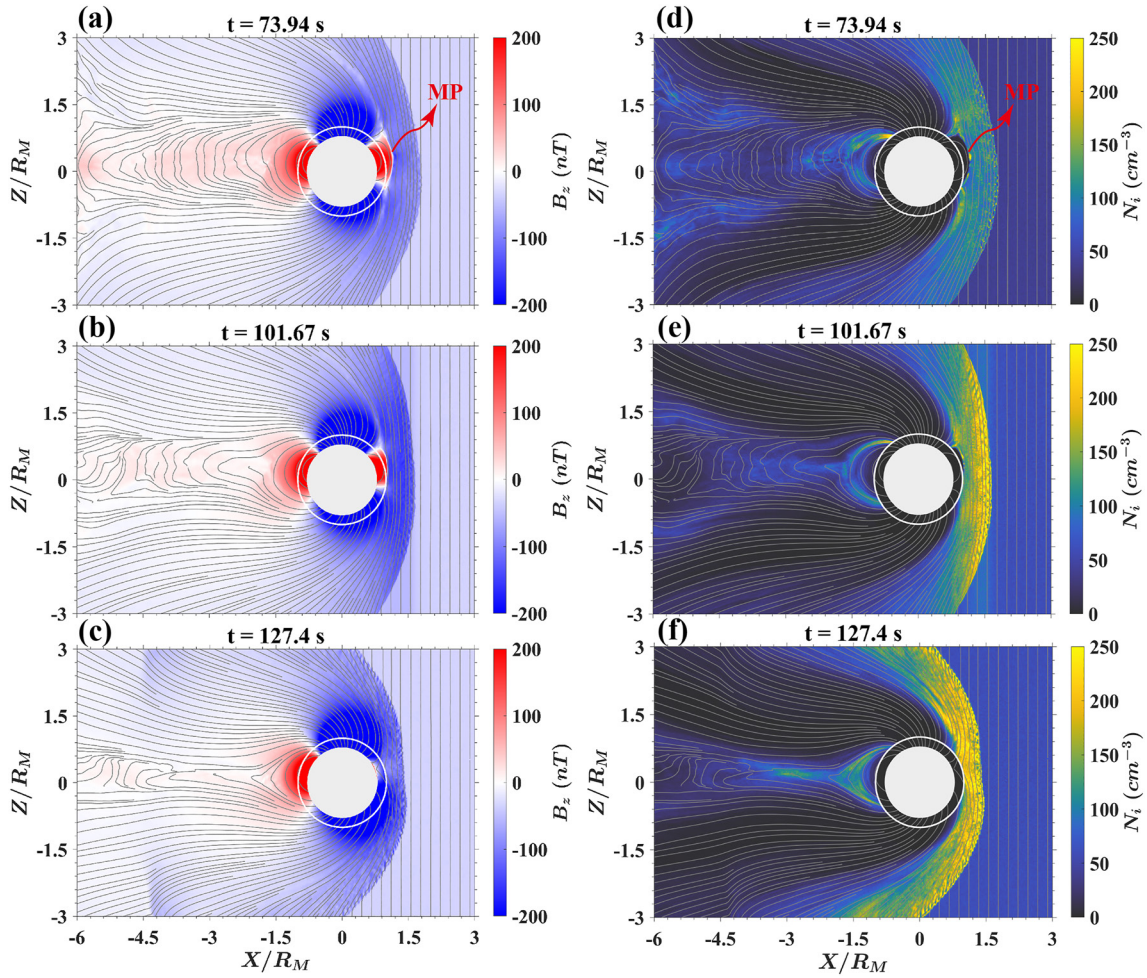

Figure 8. The evolution of the magnetosphere in the noon-midnight meridian plane obtained from Case 6. (a–c) The magnetic field lines and z component of magnetic field, B_z, at t = 73.94 s, 101.67 s, and 127.4 s. (d–f) The magnetic field lines and the ion number density, N_i, at the same time points. The magnetopause (MP) is marked by the red arrow; the surface of Mercury is indicated by the black circle; and the core of Mercury is indicated by the gray circular region.

total column abundance of Na was estimated to be 8.1×10^{11} atoms cm^{-2}. To understand the source processes of the Na exosphere of the planet, three mechanisms have been proposed: ion sputtering, photon-stimulated desorption (PSD), and meteoroid vaporization. Ion sputtering occurs when ions from the solar wind or Mercury's magnetosphere impact the planetary surface, resulting in the ejection of atomic Na with high velocity and energy (e.g., Ip, 1986; Killen et al., 1990; Killen & Morgan, 1993; Potter & Morgan, 1985, 1990, 1997). PSD occurs when solar photons hit the planetary surface and release their energy, breaking the bonds of surface materials and ejecting atomic Na from the surface (e.g., Cheng et al., 1987; McGrath et al., 1986; Peplowski et al., 2012; Wurz et al., 2010). Meteoroid vaporization occurs randomly, releasing high-energy atomic Na to high altitudes through collisions with the dust and some of the planetary surface (e.g., Cremonese et al., 2005; Morgan et al., 1988). McGrath et al. (1986) estimated that the average Na column abundance resulting from the ion sputtering is 2×10^7–2×10^8 cm^{-2}, assuming that a proton flux in cusp regions is 10^8–10^9 cm^{-2} s^{-1}. However, this value cannot account for the observed Na column density. According to the method proposed by McGrath et al. (1986), the Na column abundance (N_{col}) resulting from ion sputtering can be estimated as $\Phi f \overline{Y} \tau$. Here, Φ is the ion flux at the dayside planetary surface, f is the fractional atomic concentration of Na in the surface layer, $\overline{Y}$ is the surface-average yield, and τ is the lifetime of an Na atom in the exosphere. Under the extreme solar wind condition shown in Case 1, Φ can reach up to 10^{10} cm^{-2} s^{-1} (see Figure 4a). Taking the values of f, $\overline{Y}$, and τ as 0.002, 0.1, and 1,000 s, respectively, the N_{col} resulting from ion sputtering is about 2×10^9 cm^{-2}. However, this estimated N_{col} during the DDM event is more than two orders of magnitude lower than the observed value of 8.1×10^{11} cm^{-2}. Additionally, according to the method suggested by Sun et al. (2022), the exospheric surface

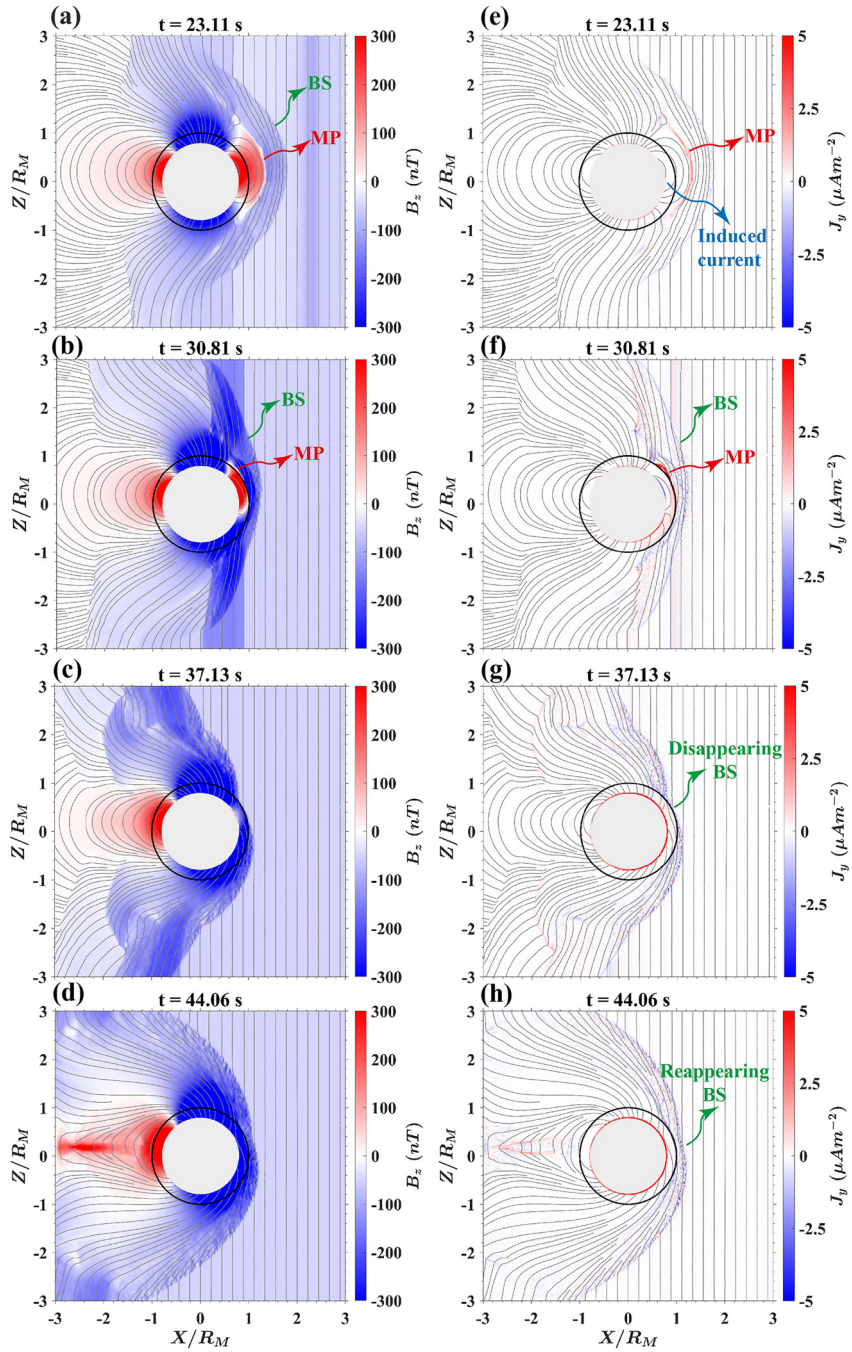

Figure 9. The evolution of the magnetopause and the bow shock in the noon-midnight meridian plane obtained from Case 7. (a–d) The magnetic field lines and the z component of magnetic field, B_z, at t = 18.49 s, 30.81 s, 37.13 s, and 52.53 s. (e–h) The magnetic field lines and the y component of current density J_y at the same time points. The rests are in the same format as Figure 2.

density of atomic Na (N_{surf}) resulting from ion sputtering can be estimated as $N_{surf} = \Phi f \overline{Y}/v_{release} = 7$ cm^{-3}, where $v_{release}$ is considered to be 3×10^5 cm s^{-1}. This estimated N_{surf} is also more than two orders of magnitude less than the observed value of 10^3–10^5 cm^{-3} in the dayside hemisphere (Cassidy et al., 2015). Taking into account the maximum value of f to be 0.06 (Peplowski et al., 2014), the maximum N_{surf} is 2×10^2 cm^{-3}, which is still less than the observed maximum N_{surf} of 10^5 cm^{-3} on the dayside hemisphere. The ion flux near the terminator can reach up to 10^9 cm^{-2} s^{-1}, and the maximum N_{surf} near the terminator is 20 cm^{-3}. This value is also less than

the observed maximum N_{surf} of 10^4 cm^{-3} near the terminator (Cassidy et al., 2015). Therefore, ion sputtering may not be the primary source mechanism for the exospheric Na of Mercury even during the DDM events. The DDM events and its influence on the changes of Na in Mercury's exosphere will be further studied by the BepiColombo mission orbiting Mercury in 2025.

5. Conclusions

In this study, we investigate the DDM events at Mercury during extreme solar wind conditions using a 3-D global hybrid simulation model. When the dynamic pressure of the solar wind is 107 nPa and the magnitude of the purely southward IMF is 50 nT, most of the dayside magnetosphere disappears within 10 s of the interaction between the solar wind and planetary magnetic field. As a consequence, about 26% of the dayside surface of Mercury is in contact with the magnetosheath. The dayside bow shock mostly disappears at about $t = 17.69$ s before the initiation of magnetotail reconnection. After the magnetotail reconnection is triggered, the magnetic flux returns to the dayside magnetosphere, and the dayside bow shock reappears at about $t = 26.42$ s. Due to the disappearance of the dayside magnetosphere, the ion flux is significantly enhanced at most of the planetary dayside surface and reaches its maximum value of about 10^{10} cm^{-2} s^{-1} at the low-latitude surface, which is much larger than that under normal solar wind conditions. However, it is still insufficient to explain the observed Na column abundance through ion sputtering.

The temporal evolution of magnetopause standoff distance under different solar wind conditions is also studied. When the solar wind dynamic pressure exceeds 25 nPa and the IMF is purely southward, part of the dayside magnetosphere disappears. The magnetopause standoff distance ($z = 0.2R_M$) reaches $1R_M$ at $t = 27$ and 58 s when the solar wind dynamic pressure is 25 and 56 nPa, respectively. Under the same IMF, the higher the solar wind dynamic pressure, the faster the magnetopause standoff distance reaches the planetary surface. When the solar wind conditions are normal (with a dynamic pressure of 8 nPa and a purely southward IMF), the dayside magnetosphere does not disappear, and the magnetopause standoff distance stabilizes at $1.15R_M$ after the magnetotail has been formed well at $t = 100$ s. However, when the IMF is purely northward and the solar wind dynamic pressure is 25 nPa, the magnetopause standoff distance stabilizes at about $1.25R_M$ after $t = 23$ s due to the absence of dayside magnetopause reconnection.

Data Availability Statement

In this study, the simulation data that are used to plot the figures can all be downloaded from Guo (2023).

Acknowledgments
This research was funded by the Strategic Priority Research Program of Chinese Academy of Sciences Grant XDB41000000, the National Science Foundation of China (NSFC) Grant 42174181, 42274196, and 42241160, and ISSI-BJ International Team "Interaction between magnetic reconnection and turbulence: From the Sun to the Earth". Computer resources were provided by the Hefei Advanced Computing Center of China. James A. Slavin and Weijie Sun are supported by NASA Grant 80NSSC21K0052 and the National Science Foundation under Grant 2321595. The work of Rajkumar Hajra was funded by the Chinese Academy of Sciences "Hundred Talents Program." The authors gratefully acknowledge the data resources from the "National Space Science Data Center, National Science & Technology Infrastructure of China (http://www.nssdc.ac.cn)."

References

Ala-Lahti, M., Pulkkinen, T. I., Pfau-Kempf, Y., Grandin, M., & Palmroth, M. (2022). Energy flux through the magnetopause during flux transfer events in Hybrid-Vlasov 2D simulations. *Geophysical Research Letters*, *49*(19), e2022GL100079. https://doi.org/10.1029/2022GL100079

Alexeev, I. I., Belenkaya, E. S., Slavin, J. A., Korth, H., Anderson, B. J., Baker, D. N., et al. (2010). Mercury's magnetospheric magnetic field after the first two MESSENGER flybys. *Icarus*, *209*(1), 23–39. https://doi.org/10.1016/j.icarus.2010.01.024

Anderson, B. J., Johnson, C. L., Korth, H., Purucker, M. E., Winslow, R. M., Slavin, J. A., et al. (2011). The global magnetic field of Mercury from MESSENGER orbital observations. *Science*, *333*(6051), 1859–1862. https://doi.org/10.1126/science.1211001

Brenner, A., Pulkkinen, T. I., Al Shidi, Q., & Toth, G. (2021). Stormtime energetics: Energy transport across the magnetopause in a Global MHD simulation. *Frontiers in Astronomy and Space Sciences*, *8*. https://doi.org/10.3389/fspas.2021.756732

Broadfoot, A. L., Shemansky, D. E., & Kumar, S. (1976). Mariner 10: Mercury atmosphere. *Geophysical Research Letters*, *3*(10), 577–580. https://doi.org/10.1029/GL003i010p00577

Cassidy, T. A., Merkel, A. W., Burger, M. H., Sarantos, M., Killen, R. M., McClintock, W. E., & Vervack, R. J. (2015). Mercury's seasonal sodium exosphere: MESSENGER orbital observations. *Icarus*, *248*, 547–559. https://doi.org/10.1016/j.icarus.2014.10.037

Cheng, A., Johnson, R., Krimigis, S., & Lanzerotti, L. (1987). Magnetosphere, exosphere, and surface of Mercury. *Icarus*, *71*(3), 430–440. https://doi.org/10.1016/0019-1035(87)90038-8

Cremonese, G., Bruno, M., Mangano, V., Marchi, S., & Milillo, A. (2005). Release of neutral sodium atoms from the surface of Mercury induced by meteoroid impacts. *Icarus*, *177*(1), 122–128. https://doi.org/10.1016/j.icarus.2005.03.022

DiBraccio, G. A., Slavin, J. A., Boardsen, S. A., Anderson, B. J., Korth, H., Zurbuchen, T. H., et al. (2013). MESSENGER observations of magnetopause structure and dynamics at Mercury. *Journal of Geophysical Research: Space Physics*, *118*(3), 997–1008. https://doi.org/10.1002/jgra.50123

Dong, C., Wang, L., Hakim, A., Bhattacharjee, A., Slavin, J. A., DiBraccio, G. A., & Germaschewski, K. (2019). Global ten-moment multifluid simulations of the solar wind interaction with Mercury: From the planetary conducting core to the dynamic magnetosphere. *Geophysical Research Letters*, *46*(21), 11584–11596. https://doi.org/10.1029/2019gl083180

Dungey, J. W. (1961). Interplanetary magnetic field and the auroral zones. *Physical Review Letters*, *6*(2), 47–48. https://doi.org/10.1103/PhysRevLett.6.47

Exner, W., Heyner, D., Liuzzo, L., Motschmann, U., Shiota, D., Kusano, K., & Shibayama, T. (2018). Coronal mass ejection hits mercury: A.I.K.E.F. hybrid-code results compared to MESSENGER data. *Planetary and Space Science*, *153*, 89–99. https://doi.org/10.1016/j.pss.2017.12.016

Exner, W., Simon, S., Heyner, D., & Motschmann, U. (2020). Influence of Mercury's exosphere on the structure of the magnetosphere. *Journal of Geophysical Research: Space Physics*, *125*(7), e2019JA027691. https://doi.org/10.1029/2019ja027691

Fatemi, S., Poppe, A. R., & Barabash, S. (2020). Hybrid simulations of solar wind proton precipitation to the surface of Mercury. *Journal of Geophysical Research: Space Physics*, *125*(4), e2019JA027706. https://doi.org/10.1029/2019ja027706

Gershman, D. J., Raines, J. M., Slavin, J. A., Zurbuchen, T. H., Sundberg, T., Boardsen, S. A., et al. (2015). MESSENGER observations of multiscale Kelvin-Helmholtz vortices at Mercury. *Journal of Geophysical Research: Space Physics*, *120*(6), 4354–4368. https://doi.org/10.1002/2014ja020903

Glassmeier, K.-H., Grosser, J., Auster, U., Constantinescu, D., Narita, Y., & Stellmach, S. (2007). Electromagnetic induction effects and dynamo action in the Hermean system. *Space Science Reviews*, *132*(2–4), 511–527. https://doi.org/10.1007/s11214-007-9244-9

Guo, J. (2023). Data for three-dimensional global hybrid simulations of Mercury's disappearing dayside magnetosphere (version V2) [Dataset]. Science Data Bank. https://doi.org/10.57760/SCIENCEDB.SPACE.00862

Guo, J., Lu, S., Lu, Q., Lin, Y., Wang, X., Huang, K., et al. (2021). Structure and coalescence of magnetopause flux ropes and their dependence on IMF clock angle: Three-dimensional global hybrid simulations. *Journal of Geophysical Research: Space Physics*, *126*(2), e2020JA028670. https://doi.org/10.1029/2020ja028670

Guo, J., Wang, B., Lu, S., Lu, Q., Lin, Y., Wang, X., et al. (2022). Azimuthal motion of poleward moving auroral forms. *Geophysical Research Letters*, *49*(16). https://doi.org/10.1029/2022gl099753

Heyner, D., Nabert, C., Liebert, E., & Glassmeier, K. H. (2016). Concerning reconnection-induction balance at the magnetopause of Mercury. *Journal of Geophysical Research: Space Physics*, *121*(4), 2935–2961. https://doi.org/10.1002/2015ja021484

Hood, L. L., & Schubert, G. (1979). Inhibition of solar wind impingement on mercury by planetary induction currents. *Journal of Geophysical Research*, *84*(A6), 2641–2647. https://doi.org/10.1029/JA084iA06p02641

Ip, W. H. (1986). The sodium exosphere and magnetosphere of Mercury. *Geophysical Research Letters*, *13*(5), 423–426. https://doi.org/10.1029/GL013i005p00423

Jia, X., Slavin, J. A., Gombosi, T. I., Daldorff, L. K. S., Toth, G., & Holst, B. (2015). Global MHD simulations of Mercury's magnetosphere with coupled planetary interior: Induction effect of the planetary conducting core on the global interaction. *Journal of Geophysical Research: Space Physics*, *120*(6), 4763–4775. https://doi.org/10.1002/2015ja021143

Jia, X., Slavin, J. A., Poh, G., DiBraccio, G. A., Toth, G., Chen, Y., et al. (2019). MESSENGER observations and global simulations of highly compressed magnetosphere events at Mercury. *Journal of Geophysical Research: Space Physics*, *124*(1), 229–247. https://doi.org/10.1029/2018ja026166

Juusola, L., Østgaard, N., & Tanskanen, E. (2011). Statistics of plasma sheet convection. *Journal of Geophysical Research*, *116*(A8), A08201. https://doi.org/10.1029/2011ja016479

Juusola, L., Østgaard, N., Tanskanen, E., Partamies, N., & Snekvik, K. (2011). Earthward plasma sheet flows during substorm phases. *Journal of Geophysical Research*, *116*(A10), A10228. https://doi.org/10.1029/2011ja016852

Kabin, K. (2000). Interaction of Mercury with the solar wind. *Icarus*, *143*(2), 397–406. https://doi.org/10.1006/icar.1999.6252

Kabin, K., Heimpel, M. H., Rankin, R., Aurnou, J. M., Gómez-Pérez, N., Paral, J., et al. (2008). Global MHD modeling of Mercury's magnetosphere with applications to the MESSENGER mission and dynamo theory. *Icarus*, *195*(1), 1–15. https://doi.org/10.1016/j.icarus.2007.11.028

Kallio, E., & Janhunen, P. (2003). Solar wind and magnetospheric ion impact on Mercury's surface. *Geophysical Research Letters*, *30*(17), 1877. https://doi.org/10.1029/2003gl017842

Kidder, A., Winglee, R. M., & Harnett, E. M. (2008). Erosion of the dayside magnetosphere at Mercury in association with ion outflows and flux rope generation. *Journal of Geophysical Research*, *113*(A9), A09223. https://doi.org/10.1029/2008ja013038

Killen, R., Potter, A., & Morgan, T. (1990). Spatial distribution of sodium vapor in the atmosphere of Mercury. *Icarus*, *85*(1), 145–167. https://doi.org/10.1016/0019-1035(90)90108-L

Killen, R. M., & Morgan, T. H. (1993). Maintaining the Na atmosphere of Mercury. *Icarus*, *101*(2), 293–312. https://doi.org/10.1006/icar.1993.1026

Korth, H., Anderson, B. J., Johnson, C. L., Slavin, J. A., Raines, J. M., & Zurbuchen, T. H. (2018). Structure and configuration of Mercury's magnetosphere. In *Mercury* (pp. 430–460). https://doi.org/10.1017/9781316650684.017

Lapenta, G., Schriver, D., Walker, R. J., Berchem, J., Echterling, N. F., El Alaoui, M., & Travnicek, P. (2022). Do we need to consider electrons' kinetic effects to properly model a planetary magnetosphere: The case of Mercury. *Journal of Geophysical Research: Space Physics*, *127*(4), e2021JA030241. https://doi.org/10.1029/2021ja030241

Le, G., Chi, P. J., Blanco-Cano, X., Boardsen, S., Slavin, J. A., Anderson, B. J., & Korth, H. (2013). Upstream ultra-low frequency waves in Mercury's foreshock region: MESSENGER magnetic field observations. *Journal of Geophysical Research: Space Physics*, *118*(6), 2809–2823. https://doi.org/10.1002/jgra.50342

Li, C., Jia, X., Chen, Y., Toth, G., Zhou, H., Slavin, J. A., et al. (2023). Global hall MHD simulations of Mercury's magnetopause dynamics and FTEs under different solar wind and IMF conditions. *Journal of Geophysical Research: Space Physics*, *128*(5), e2022JA031206. https://doi.org/10.1029/2022ja031206

Liljeblad, E., Sundberg, T., Karlsson, T., & Kullen, A. (2014). Statistical investigation of Kelvin-Helmholtz waves at the magnetopause of Mercury. *Journal of Geophysical Research: Space Physics*, *119*(12), 9670–9683. https://doi.org/10.1002/2014ja020614

Liu, Y. H., Li, T. C., Hesse, M., Sun, W. J., Liu, J., Burch, J., et al. (2019). Three-dimensional magnetic reconnection with a spatially confined X-line extent: Implications for dipolarizing flux bundles and the dawn-dusk asymmetry. *Journal of Geophysical Research: Space Physics*, *124*(4), 2819–2830. https://doi.org/10.1029/2019ja026539

Lu, Q., Guo, J., Lu, S., Wang, X., Slavin, J. A., Sun, W., et al. (2022). Three-dimensional global hybrid simulations of flux transfer event showers at Mercury. *The Astrophysical Journal*, *937*(1), 1. https://doi.org/10.3847/1538-4357/ac8bcf

Lu, Q., Ke, Y., Wang, X., Liu, K., Gao, X., Chen, L., & Wang, S. (2019). Two-dimensional gcPIC simulation of rising-tone chorus waves in a dipole magnetic field. *Journal of Geophysical Research: Space Physics*, *124*(6), 4157–4167. https://doi.org/10.1029/2019ja026586

McGrath, M., Johnson, R., & Lanzerotti, L. (1986). Sputtering of sodium on the planet Mercury. *Nature*, *323*(6090), 694–696. https://doi.org/10.1038/323694a0

Morgan, T., Zook, H., & Potter, A. (1988). Impact-driven supply of sodium and potassium to the atmosphere of Mercury. *Icarus*, *75*(1), 156–170. https://doi.org/10.1016/0019-1035(88)90134-0

Müller, J., Simon, S., Wang, Y.-C., Motschmann, U., Heyner, D., Schüle, J., et al. (2012). Origin of Mercury's double magnetopause: 3D hybrid simulation study with A.I.K.E.F. *Icarus*, *218*(1), 666–687. https://doi.org/10.1016/j.icarus.2011.12.028

Ness, N. F., Behannon, K. W., Lepping, R. P., Whang, Y. C., & Schatten, K. H. (1974). Magnetic field observations near Mercury: Preliminary results from mariner 10. *Science*, *185*(4146), 151–160. https://doi.org/10.1126/science.185.4146.151

Peplowski, P. N., Evans, L. G., Stockstill-Cahill, K. R., Lawrence, D. J., Goldsten, J. O., McCoy, T. J., et al. (2014). Enhanced sodium abundance in Mercury's North Polar Region revealed by the MESSENGER Gamma-Ray Spectrometer. *Icarus*, *228*, 86–95. https://doi.org/10.1016/j.icarus.2013.09.007

Peplowski, P. N., Lawrence, D. J., Rhodes, E. A., Sprague, A. L., McCoy, T. J., Denevi, B. W., et al. (2012). Variations in the abundances of potassium and thorium on the surface of Mercury: Results from the MESSENGER Gamma-Ray spectrometer. *Journal of Geophysical Research*, *117*(E12), E00L04. https://doi.org/10.1029/2012je004141

Poh, G., Slavin, J. A., Jia, X., DiBraccio, G. A., Raines, J. M., Imber, S. M., et al. (2016). MESSENGER observations of cusp plasma filaments at Mercury. *Journal of Geophysical Research: Space Physics*, *121*(9), 8260–8285. https://doi.org/10.1002/2016ja022552

Potter, A., & Morgan, T. (1985). Discovery of sodium in the atmosphere of Mercury. *Science*, *229*(4714), 651–653. https://doi.org/10.1126/science.229.4714.651

Potter, A., & Morgan, T. (1997). Sodium and potassium atmospheres of Mercury. *Planetary and Space Science*, *45*(1), 95–100. https://doi.org/10.1016/S0032-0633(96)00100-6

Potter, A. E., & Morgan, T. H. (1990). Evidence for magnetospheric effects on the sodium atmosphere of Mercury. *Science*, *248*(4957), 835–838. https://doi.org/10.1126/science.248.4957.835

Raines, J. M., Dewey, R. M., Staudacher, N. M., Tracy, P. J., Bert, C. M., Sarantos, M., et al. (2022). Proton precipitation in Mercury's northern magnetospheric cusp. *Journal of Geophysical Research: Space Physics*, *127*(11), e2022JA030397. https://doi.org/10.1029/2022ja030397

Romanelli, N., DiBraccio, G., Gershman, D., Le, G., Mazelle, C., Meziane, K., et al. (2020). Upstream ultra-low frequency waves observed by MESSENGER's magnetometer: Implications for particle acceleration at Mercury's bow shock. *Geophysical Research Letters*, *47*(9), e2020GL087350. https://doi.org/10.1029/2020gl087350

Romanelli, N., & DiBraccio, G. A. (2021). Occurrence rate of ultra-low frequency waves in the foreshock of Mercury increases with heliocentric distance. *Nature Communications*, *12*(1), 6748. https://doi.org/10.1038/s41467-021-26344-2

Shi, Z., Rong, Z. J., Fatemi, S., Slavin, J. A., Klinger, L., Dong, C., et al. (2022). An eastward current encircling Mercury. *Geophysical Research Letters*, *49*(10), e2022GL098415. https://doi.org/10.1029/2022gl098415

Slavin, J. A., Acuña, M. H., Anderson, B. J., Baker, D. N., Benna, M., Boardsen, S. A., et al. (2009). MESSENGER observations of magnetic reconnection in Mercury's magnetosphere. *Science*, *324*(5927), 606–610. https://doi.org/10.1126/science.1172011

Slavin, J. A., Acuña, M. H., Anderson, B. J., Baker, D. N., Benna, M., Gloeckler, G., et al. (2008). Mercury's magnetosphere after MESSENGER's first flyby. *Science*, *321*(5885), 85–89. https://doi.org/10.1126/science.1159040

Slavin, J. A., Anderson, B. J., Baker, D. N., Benna, M., Boardsen, S. A., Gloeckler, G., et al. (2010). MESSENGER observations of extreme loading and unloading of Mercury's magnetic tail. *Science*, *329*(5992), 665–668. https://doi.org/10.1126/science.1188067

Slavin, J. A., DiBraccio, G. A., Gershman, D. J., Imber, S. M., Poh, G. K., Raines, J. M., et al. (2014). MESSENGER observations of Mercury's dayside magnetosphere under extreme solar wind conditions. *Journal of Geophysical Research: Space Physics*, *119*(10), 8087–8116. https://doi.org/10.1002/2014ja020319

Slavin, J. A., Imber, S. M., Boardsen, S. A., DiBraccio, G. A., Sundberg, T., Sarantos, M., et al. (2012). MESSENGER observations of a flux-transfer-event shower at Mercury. *Journal of Geophysical Research*, *117*(A12), A00M06. https://doi.org/10.1029/2012ja017926

Slavin, J. A., Lepping, R. P., Wu, C.-C., Anderson, B. J., Baker, D. N., Benna, M., et al. (2010). MESSENGER observations of large flux transfer events at Mercury. *Geophysical Research Letters*, *37*(2). https://doi.org/10.1029/2009gl041485

Slavin, J. A., Middleton, H. R., Raines, J. M., Jia, X., Zhong, J., Sun, W. J., et al. (2019). MESSENGER observations of disappearing dayside magnetosphere events at Mercury. *Journal of Geophysical Research: Space Physics*, *124*(8), 6613–6635. https://doi.org/10.1029/2019ja026892

Smith, A. W., Slavin, J. A., Jackman, C. M., Poh, G. K., & Fear, R. C. (2017). Flux ropes in the Hermean magnetotail: Distribution, properties, and formation. *Journal of Geophysical Research: Space Physics*, *122*(8), 8136–8153. https://doi.org/10.1002/2017ja024295

Smith, D. E., Zuber, M. T., Phillips, R. J., Solomon, S. C., Hauck, S. A., Lemoine, F. G., et al. (2012). Gravity field and internal structure of Mercury from MESSENGER. *Science*, *336*(6078), 214–217. https://doi.org/10.1126/science.1218809

Spreiter, J. R., Summers, A. L., & Alksne, A. Y. (1966). Hydromagnetic flow around the magnetosphere. *Planetary and Space Science*, *14*(3), 223–253. https://doi.org/10.1016/0032-0633(66)90124-3

Suess, S. T., & Goldstein, B. E. (1979). Compression of the Hermaean magnetosphere by the solar wind. *Journal of Geophysical Research*, *84*(A7), 3306–3312. https://doi.org/10.1029/JA084iA07p03306

Sun, W., Dewey, R. M., Aizawa, S., Huang, J., Slavin, J. A., Fu, S., et al. (2021). Review of Mercury's dynamic magnetosphere: Post-MESSENGER era and comparative magnetospheres. *Science China Earth Sciences*, *65*(1), 25–74. https://doi.org/10.1007/s11430-021-9828-0

Sun, W., Slavin, J. A., Milillo, A., Dewey, R. M., Orsini, S., Jia, X., et al. (2022). MESSENGER observations of planetary ion enhancements at Mercury's northern magnetospheric cusp during flux transfer event showers. *Journal of Geophysical Research: Space Physics*, *127*(4), e2022JA030280. https://doi.org/10.1029/2022JA030280

Sun, W. J., Fu, S. Y., Slavin, J. A., Raines, J. M., Zong, Q. G., Poh, G. K., & Zurbuchen, T. H. (2016). Spatial distribution of Mercury's flux ropes and reconnection fronts: MESSENGER observations. *Journal of Geophysical Research: Space Physics*, *121*(8), 7590–7607. https://doi.org/10.1002/2016ja022787

Sun, W. J., Fu, S. Y., Wei, Y., Yao, Z. H., Rong, Z. J., Zhou, X. Z., et al. (2017). Plasma sheet pressure variations in the near-Earth magnetotail during substorm growth phase: THEMIS observations. *Journal of Geophysical Research: Space Physics*, *122*(12), 12212–212228. https://doi.org/10.1002/2017ja024603

Sun, W. J., Slavin, J. A., Smith, A. W., Dewey, R. M., Poh, G. K., Jia, X., et al. (2020). Flux transfer event showers at Mercury: Dependence on plasma β and magnetic shear and their contribution to the dungey cycle. *Geophysical Research Letters*, *47*(21). https://doi.org/10.1029/2020gl089784

Sundberg, T., Boardsen, S. A., Slavin, J. A., Blomberg, L. G., Cumnock, J. A., Solomon, S. C., et al. (2011). Reconstruction of propagating Kelvin–Helmholtz vortices at Mercury's magnetopause. *Planetary and Space Science*, *59*(15), 2051–2057. https://doi.org/10.1016/j.pss.2011.05.008

Trávníček, P., Hellinger, P., & Schriver, D. (2007). Structure of Mercury's magnetosphere for different pressure of the solar wind: Three dimensional hybrid simulations. *Geophysical Research Letters*, *34*(5). https://doi.org/10.1029/2006gl028518

Trávníček, P. M., Schriver, D., Hellinger, P., Herčík, D., Anderson, B. J., Sarantos, M., & Slavin, J. A. (2010). Mercury's magnetosphere–solar wind interaction for northward and southward interplanetary magnetic field: Hybrid simulation results. *Icarus*, *209*(1), 11–22. https://doi.org/10.1016/j.icarus.2010.01.008

Varela, J., Pantellini, F., & Moncuquet, M. (2015). The effect of interplanetary magnetic field orientation on the solar wind flux impacting Mercury's surface. *Planetary and Space Science*, *119*, 264–269. https://doi.org/10.1016/j.pss.2015.10.004

Wang, Y. C., Mueller, J., Motschmann, U., & Ip, W. H. (2010). A hybrid simulation of Mercury's magnetosphere for the MESSENGER encounters in year 2008. *Icarus*, *209*(1), 46–52. https://doi.org/10.1016/j.icarus.2010.05.020

Winslow, R. M., Anderson, B. J., Johnson, C. L., Slavin, J. A., Korth, H., Purucker, M. E., et al. (2013). Mercury's magnetopause and bow shock from MESSENGER Magnetometer observations. *Journal of Geophysical Research: Space Physics*, *118*(5), 2213–2227. https://doi.org/10.1002/jgra.50237

Winslow, R. M., Lugaz, N., Philpott, L., Farrugia, C. J., Johnson, C. L., Anderson, B. J., et al. (2020). Observations of extreme ICME ram pressure compressing Mercury's dayside magnetosphere to the surface. *The Astrophysical Journal*, *889*(2), 184. https://doi.org/10.3847/1538-4357/ab6170

Wurz, P., Whitby, J., Rohner, U., Martín-Fernández, J., Lammer, H., & Kolb, C. (2010). Self-consistent modelling of Mercury's exosphere by sputtering, micro-meteorite impact and photon-stimulated desorption. *Planetary and Space Science*, *58*(12), 1599–1616. https://doi.org/10.1016/j.pss.2010.08.003

Zhao, J. T., Zong, Q. G., Yue, C., Sun, W. J., Zhang, H., Zhou, X. Z., et al. (2022). Observational evidence of ring current in the magnetosphere of Mercury. *Nature Communications*, *13*(1), 924. https://doi.org/10.1038/s41467-022-28521-3

Zhong, J., Wan, W. X., Wei, Y., Slavin, J. A., Raines, J. M., Rong, Z. J., et al. (2015). Compressibility of Mercury's dayside magnetosphere. *Geophysical Research Letters*, *42*(23), 10135–10139. https://doi.org/10.1002/2015gl067063